

Three-dimensional chiral active Ornstein-Uhlenbeck model for helical motion of microorganisms

Leon Lettermann,^{1,2} Falko Ziebert,^{1,2} Mirko Singer,³ Friedrich Frischknecht,³ and Ulrich S. Schwarz^{1,2,*}

¹*Institute for Theoretical Physics, Heidelberg University, Philosophenweg 19, 69120 Heidelberg, Germany*

²*Bioquant-Center, Heidelberg University, Im Neuenheimer Feld 267, 69120 Heidelberg, Germany*

³*Parasitology, Center for Infectious Diseases, Heidelberg University, Im Neuenheimer Feld 344, 69120 Heidelberg*

(Dated: February 3, 2025)

Active movement is essential for the survival of microorganisms like bacteria, algae and unicellular parasites, for example the ones causing the disease malaria. In three dimensions, both swimming and gliding microorganisms often exhibit helical trajectories. Here we introduce a stochastic dynamics model for chiral self-propelled particles, for which both propulsion force and torque are internally generated, the latter stochastically by an Ornstein-Uhlenbeck process. We demonstrate that a truncated version of the full model can be solved analytically, in very good agreement with computer simulations for the full model. Our main result is that this model allows for larger long-time mean squared displacements for helical compared to straight 3D movement at the same speed, suggesting an evolutionary benefit of the often observed helical movements of microorganisms, and opposite to the reduction of diffusion caused by chirality in 2D. We then provide an experimental example by analyzing imaging data for malaria parasites that glide through hydrogels on helical trajectories.

The survival of microbes like bacteria or algae is tightly connected to their ability to actively move, which is essential to seek out more favorable conditions, e.g. places which offer more nutrients or sunlight for photosynthesis [1, 2]. Although sometimes movement is collective, e.g. in biofilms or during swarming, at the heart of all migration processes is always the capability of single microbes to internally generate forces and torques to generate some kind of movement [3–5]. Migration over large distances is also essential for unicellular eukaryotes that have specialized in infecting mammalian host, such as the causative agents of the diseases malaria or toxoplasmosis [6]. Interestingly, in three dimensions many microorganisms exhibit helical trajectories [7, 8]. This includes species of swimming bacteria [9, 10], swimming algae [11, 12] and gliding parasites [13–15]. In Fig. 1, we show the helical trajectories of malaria parasite moving through synthetic hydrogels (see Appendix A for experimental details).

Since the pioneering work of Berg and Purcell, it is well accepted that one of the main challenges for moving microorganisms is to counter the effects of stochastic noise [16, 17]. For example, the bacterium *E. coli* uses a run-and-tumble strategy to move up and down chemotactic gradients; here the tumble periods are believed to be required to reset the system because it tends to lose orientation during the run periods due to rotational Brownian noise [18]. The interplay of self-propulsion and external noise can be analyzed by the theory of active Brownian particles, which combines a propulsion force with stochastic noise for translation and rotation [19–22]. The active Brownian particle model has been used and extended in various contexts [23–28], including adding torques to obtain circle swimmers [29–35] and studying the influence of time-correlated noise [36–40]. However, most of these studies considered 2D cases, whereas helical motion of chiral active particles occurs in 3D [26].

One of the few studies addressing chiral motion in 3D started from the full mobility tensor for an arbitrarily shaped particle and showed that helical trajectories are the most likely outcome [41]. Helical trajectories in 3D have also been discussed before in the context of sperm chemotaxis, suggesting that helical trajectories are useful search strategies in noisy hydrodynamic environments [42, 43].

Noise does not only arise from the interaction of the microorganisms with their environment, but also from the internal force generating processes, which have a correlation time on the same scale as the movement that they generate. To address this aspect of the system, Ornstein-Uhlenbeck (OU) processes have been used, usually replacing the body-fixed constant velocity with a noisy velocity performing an OU process around a body-fixed average [44]. This naturally introduces a time scale to the noise and in the context of 2D swimmers in recent years has attracted substantial attention [45–52]. However, this approach has not yet been extended to chiral particles in 3D.

Here we introduce a three-dimensional model which

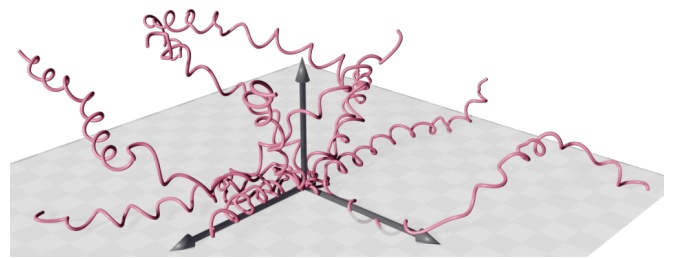


FIG. 1. Reconstructed trajectories of malaria parasites gliding through synthetic hydrogels. Because this environment is nearly isotropic, the right-handed helical trajectories persist for long times.

represents the noise in the generation of torque as an OU-process, similarly as suggested previously for 2D [53]. As we demonstrate here, this 3D-model for chiral active particles can be treated analytically by suitably truncating a hierarchy of equations. We derive equations for the effective correlation time, the mean position and the mean squared displacement (MSD). Our main finding is that for a particle moving in 3D, a helical trajectory can be "straighter than a straight line", i.e. the long-time mean squared displacement can be larger for a particle following a helical trajectory compared to a particle moving with the same speed on a straight trajectory. This is caused by the rotation averaging out parts of the noise if both have comparable time-scales, and suggests that helical trajectories are favored for microorganisms that have to quickly move large distances (many body lengths) through their environment. Finally we compare our model to experimental data from malaria parasites, demonstrating that it can describe the MSD obtained from reconstructions of the imaged trajectories as shown in Fig. 1.

Model. To model the intrinsic rotational noise we consider an active particle that is moving with a body-fixed constant translational velocity $\mathbf{V}_0^{\text{body}}$. Its rotational velocity performs an OU-process around the body-fixed average, $\mathbf{\Omega}_0^{\text{body}}$. In the lab frame we use two vectors to track the orientation of the particle. \mathbf{n}_1 is the direction of the mean angular velocity $\mathbf{\Omega}_0$ and $\mathbf{n}_2 \perp \mathbf{n}_1$ is defined with the angle α between $\mathbf{\Omega}_0$ and \mathbf{V}_0 (see Appendix Fig. A1 for a schematics):

$$\mathbf{\Omega}_0 = \Omega_0 \mathbf{n}_1, \quad \mathbf{V}_0 = |\mathbf{V}_0| (\mathbf{n}_1 \cos \alpha + \mathbf{n}_2 \sin \alpha). \quad (1)$$

For simplicity, we set $|\mathbf{V}_0| = 1$ in the following. In the lab frame, the equations of motion are

$$d\mathbf{\Omega} = -k(\mathbf{\Omega} - \Omega_0 \mathbf{n}_1) dt + h d\mathbf{\Lambda} \quad (2)$$

$$d\mathbf{n}_1 = (\mathbf{\Omega} \times \mathbf{n}_1) dt \quad (3)$$

$$d\mathbf{n}_2 = (\mathbf{\Omega} \times \mathbf{n}_2) dt \quad (4)$$

$$d\mathbf{r} = (\cos(\alpha)\mathbf{n}_1 + \sin(\alpha)\mathbf{n}_2) dt. \quad (5)$$

Here, k is the potential strength and h the noise amplitude of the OU process. $d\mathbf{\Lambda}$ is a 3D standard Wiener process. Note that noise is not multiplicative in the lab frame. Focusing on the intrinsic noise for simplicity, we disregard external noise (such as Brownian translational noise) or intrinsic noise in the translational velocity.

Rotation. The rotational part described by Eq. 2-3 is decoupled from the rest and can be solved first. The dynamical equations for the averages $\langle \mathbf{\Omega}_0 \rangle$ and $\langle \mathbf{n}_1 \rangle$ constitute an infinite hierarchy of expectation values of cross products of these two quantities, the first four being

$$d\langle \mathbf{\Omega} \rangle = -k(\langle \mathbf{\Omega} \rangle - \Omega_0 \langle \mathbf{n}_1 \rangle) dt \quad (6)$$

$$d\langle \mathbf{n}_1 \rangle = \langle \mathbf{\Omega} \times \mathbf{n}_1 \rangle dt \quad (7)$$

$$d\langle \mathbf{\Omega} \times \mathbf{n}_1 \rangle = -k\langle \mathbf{\Omega} \times \mathbf{n}_1 \rangle dt + \langle \mathbf{\Omega} \times (\mathbf{\Omega} \times \mathbf{n}_1) \rangle dt \quad (8)$$

and

$$\begin{aligned} d\langle \mathbf{\Omega} \times (\mathbf{\Omega} \times \mathbf{n}_1) \rangle &= -2k\langle \mathbf{\Omega} \times (\mathbf{\Omega} \times \mathbf{n}_1) \rangle dt \\ &+ \langle \mathbf{\Omega} \times (\mathbf{\Omega} \times (\mathbf{\Omega} \times \mathbf{n}_1)) \rangle dt \\ &+ k\Omega_0 \langle \mathbf{n}_1 \times (\mathbf{\Omega} \times \mathbf{n}_1) \rangle dt \\ &+ h^2 \langle d\mathbf{\Lambda} \times (d\mathbf{\Lambda} \times \mathbf{n}_1) \rangle. \end{aligned}$$

To obtain an analytical solution, we have to make approximations for the second and third term in this equation to truncate the hierarchy. First, assuming $\langle \mathbf{\Omega}^2 A \rangle \approx \Omega_0^2 \langle A \rangle$, we get for the second term $\langle \mathbf{\Omega} \times (\mathbf{\Omega} \times (\mathbf{\Omega} \times \mathbf{n}_1)) \rangle \approx -\Omega_0^2 \langle \mathbf{\Omega} \times \mathbf{n}_1 \rangle$. For the third term, upon replacing $\mathbf{\Omega}$ with $\mathbf{\Omega}^\perp$, its component perpendicular to \mathbf{n}_1 , the relevant contribution for the cross product, and applying similar logic as before but with $|\mathbf{n}_1| = 1$, we get $\langle \mathbf{n}_1 \times (\mathbf{\Omega} \times \mathbf{n}_1) \rangle = \langle \mathbf{\Omega}^\perp \rangle = \langle \mathbf{\Omega} - (\mathbf{\Omega} \cdot \mathbf{n}_1)\mathbf{n}_1 \rangle \approx \langle \mathbf{\Omega} \rangle - \Omega_0 \langle \mathbf{n}_1 \rangle$. For the last approximation, we assumed that the variance of the OU process is small, such that $\mathbf{\Omega}$ stays close to its average $\Omega_0 \mathbf{n}_1$. The noise term can be explicitly computed, and we can close the hierarchy by rewriting its fourth equation as

$$\begin{aligned} d\langle \mathbf{\Omega} \times (\mathbf{\Omega} \times \mathbf{n}_1) \rangle &= -2k\langle \mathbf{\Omega} \times (\mathbf{\Omega} \times \mathbf{n}_1) \rangle dt \quad (9) \\ &- \Omega_0^2 \langle \mathbf{\Omega} \times \mathbf{n}_1 \rangle dt + k\Omega_0 (\langle \mathbf{\Omega} \rangle - \Omega_0 \langle \mathbf{n}_1 \rangle) dt - 2h^2 \langle \mathbf{n}_1 \rangle dt. \end{aligned}$$

By rotational symmetry, only the component singled out by the initially parallel $\mathbf{\Omega}$ and \mathbf{n}_1 axes is relevant (as the rotational problem is independent of \mathbf{n}_2), and the other two components of each vector vanish upon averaging (we choose this direction to be z). Hence, the truncated system defines a four-dimensional, homogeneous ordinary differential equation problem, which we can analyze by its eigenvalues (see Appendix B for the truncation in the case of vanishing Ω_0).

The mode relevant for the long time behavior can be identified as the unique mode with real eigenvalue and parallel $\langle \mathbf{\Omega} \rangle$ and $\langle \mathbf{n}_1 \rangle$, which describes the decorrelation of $\langle \mathbf{\Omega} \rangle$ from its initial orientation. The other eigenvalues describe the unstable state where $\mathbf{\Omega}$, \mathbf{n}_1 are anti-parallel, and oscillatory states which decay more quickly. The relevant eigenvalue can be computed exactly, but as a solution of a fourth-order polynomial, it is cumbersome. Expanding for small k/Ω_0 , i.e. assuming the rotation is faster than the timescale on which the OUP returns to its average, we get the approximation

$$\lambda = -\frac{h^2 + \Omega_0^2 k + k^3 - \sqrt{k^2 (\Omega_0^2 + k^2)^2 - h^4}}{\Omega_0^2 + k^2} \quad (10)$$

which describes the decay as $\langle \mathbf{\Omega} \rangle = (0, 0, \Omega_0) \exp(\lambda t)$ and $\langle \mathbf{n}_1 \rangle = (0, 0, 1) \exp(\lambda t)$. The more negative λ , the faster $\mathbf{\Omega}$ and \mathbf{n}_1 decorrelate from their initial orientation. For fixed noise amplitude h , both decreasing the strength k of the OUP potential and decreasing angular speed Ω_0 lead to faster decorrelation, suggesting that the rotation has a stabilizing effect. In the limits of vanishing noise,

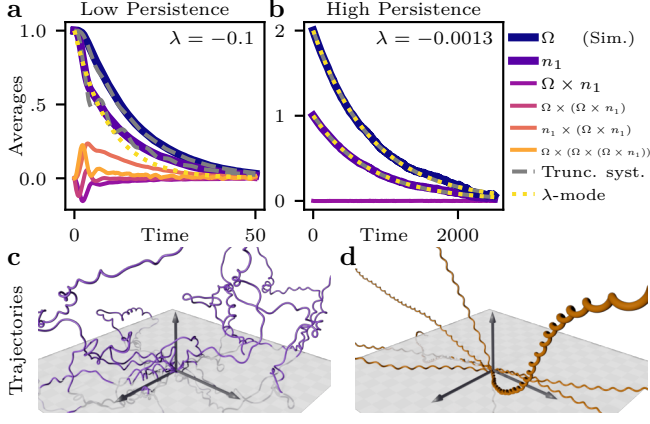


FIG. 2. **a**: Time course of expectation values of different quantities obtained from numerical simulation (Eq. 2-5) in comparison with numerical solution of the truncated system (Eq. 6-9, gray dashed lines) and analytical approximation predicting exponential decay with eigenvalue λ (Eq. 10, yellow dotted lines). Parameter values: potential strength $k = 0.2$, noise amplitude $h = 0.3$, angular speed $\Omega_0 = 1$, angle $\alpha = \pi/6$. **b**: Same as a, but now for $k = 2$, $h = 0.1$ and $\Omega_0 = 2$, i.e. much reduced noise and faster turning. Here, the agreement between simulations and theory is even better. **c**: Simulated trajectories at parameters from a. **d**: Simulated trajectories at parameters from b. The reduced noise leads to more regular trajectories.

diverging potential strength or diverging angular speed, the time scale of decorrelation diverges.

To validate our approximations, we compared the solutions against numerical simulations of the initial model (Eq. 2-5, implemented in JAX [54] using standard solvers for stochastic differential equations, set up in diffrax [55]). In Fig. 2, different expectation values obtained from averaging 20,000 numerical simulations are compared with (i) the numerically solved truncated ODE system (Eq. 6-9, dashed gray) and (ii) the analytical exponential decay given by the dominant eigenvalue λ . As shown in Fig. 2a, larger noise yielding faster decorrelation produces larger values of the higher order expectation values. We find that the truncations are qualitatively correct, while quantitative differences are visible – the numerical solution of the truncated system shows some additional oscillations. The exponential decay by λ is too fast here, which signifies that during the relatively rapid decay, additional modes are relevant. For lower noise, in Fig. 2b we see excellent agreement between numerical simulation, numerical solution of the truncated system, and the exponential decay given by λ from Eq. 10. The latter decay completely dictates the persistence in the resulting motion, as also apparent in the resulting trajectories illustrated in Fig. 2c+d. Generally, lower decorrelation can be reached by lower noise amplitude h , stronger Ornstein-Uhlenbeck potential k , or higher angular speed Ω_0 .

Translation. For the translational part, we assume that initially $\mathbf{\Omega} = \Omega_0 \mathbf{n}_1$ is in z direction. The solution of the rotational part then allows to solve Eq. 5 for the motion in z , $d\langle z \rangle = \cos(\alpha) \langle \mathbf{n}_1 \rangle$. To obtain the MSD and the remaining coordinate, we need an expression for $\langle \mathbf{n}_2 \rangle$. By construction, $\mathbf{n}_2 \perp \mathbf{n}_1$, so \mathbf{n}_2 is rotating in the plane perpendicular to \mathbf{n}_1 with angular frequency Ω_0 , which is on average the x - y -plane. We assume that \mathbf{n}_2 initially points in x -direction. The decorrelation of \mathbf{n}_1 is also decorrelating the plane in which \mathbf{n}_2 rotates, but the latter additionally decorrelates within the plane by variations of the magnitude of the rotational velocity. Both effects are caused by $\mathbf{\Omega}$ deviating from $\mathbf{\Omega}_0$, the tilting of the plane by deviations perpendicular to $\mathbf{\Omega}_0$, and in-plane deviations by parallel components. Because of this additional effect, we obtain a two-fold faster decorrelation of $\langle \mathbf{n}_2 \rangle$ compared to $\langle \mathbf{n}_1 \rangle$ (see Appendix C for more details),

$$\langle \mathbf{n}_2 \rangle = (\cos \Omega_0 t, \sin \Omega_0 t, 0) e^{2\lambda t}. \quad (11)$$

The MSD can now be obtained (see Appendix D) by first computing it from the formal solution and inserting the solutions obtained for $\langle \mathbf{n}_1 \rangle$ and $\langle \mathbf{n}_2 \rangle$. The result is (except for the degenerate case $\Omega_0 = 0$ and $\alpha > 0$):

$$\begin{aligned} \langle \mathbf{r}_t^2 \rangle &= \frac{2 \cos^2(\alpha) (-\lambda t + e^{\lambda t} - 1)}{\lambda^2} \\ &+ \frac{2 \sin^2(\alpha)}{(4\lambda^2 + \Omega_0^2)^2} \left[-4\lambda^2 + \Omega_0^2 - 2\lambda(4\lambda^2 + \Omega_0^2)t \right. \\ &\left. + (4\lambda^2 - \Omega_0^2) e^{2\lambda t} \cos(\Omega_0 t) + 4\lambda\Omega_0 e^{2\lambda t} \sin(\Omega_0 t) \right]. \end{aligned} \quad (12)$$

Let us consider two limiting cases. First, for $\alpha = 0$, corresponding to a particle rotating while traveling on a straight line, we obtain

$$\langle \mathbf{r}_t^2 \rangle = \frac{2(-\lambda t + e^{\lambda t} - 1)}{\lambda^2}. \quad (13)$$

For general α in the limit of large t we can approximate $\langle \mathbf{r}_t^2 \rangle \approx 6Dt$, where we obtain the effective diffusion constant describing the long time behavior as

$$D = -\frac{\lambda}{3} \left(\frac{\cos^2(\alpha)}{\lambda^2} + \frac{2 \sin^2(\alpha)}{(4\lambda^2 + \Omega_0^2)} \right). \quad (14)$$

In the case $\lambda^2 \ll \Omega_0^2$, meaning small noise leading to a decay time much longer than the rotation period, and $\alpha < \pi/2$, i.e. the particle not just circling, but having some average net movement, this reduces to $D \approx -\cos^2(\alpha)/(3\lambda)$.

Lastly, with Eq. 11 we compute $\langle x \rangle$ and $\langle y \rangle$ by integrating $d\langle x \rangle = \sin(\alpha) \langle \mathbf{n}_2 \rangle_x dt$, allowing to obtain the expectation value of the trajectory,

$$\langle \mathbf{r}(t) \rangle = \begin{pmatrix} \sin(\alpha) \frac{e^{2\lambda t} (2\lambda \cos(\Omega_0 t) + \Omega_0 \sin(\Omega_0 t)) - 2\lambda}{4\lambda^2 + \Omega_0^2} \\ \sin(\alpha) \frac{e^{2\lambda t} (2\lambda \sin(\Omega_0 t) - \Omega_0 \cos(\Omega_0 t)) + \Omega_0}{4\lambda^2 + \Omega_0^2} \\ \frac{\cos(\alpha)}{\lambda} (e^{\lambda t} - 1) \end{pmatrix}, \quad (15)$$

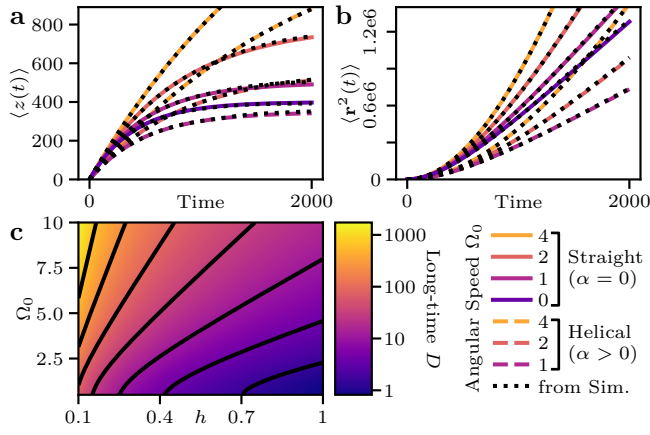


FIG. 3. **a**: Mean distance traveled in z -direction (the initial orientation of the helical axis) for different Ω_0 at $k = 2$, $h = 0.1$. Full lines show particles moving straight while turning ($\alpha=0$), dashed lines particles on helical trajectories ($\alpha=\pi/4$), which can be seen overtaking slower turning straight particles. Colored and black lines are theoretical and numerical, respectively, and in very good agreement. **b**: Mean squared displacement for the same parameters as shown in a, theoretical results from Eq. 12 in color. **c**: Effective long-time diffusion constant D , cf. Eq. 14, as a function of noise amplitude h and angular speed Ω_0 . Black lines mark contours of constant D .

which is a logarithmic spiral on a radical surface, i.e. $z \propto \sqrt{r}$.

Results. The derived solutions show that increasing rotation Ω_0 stabilizes the particle against its intrinsic noise. In Fig. 3a and b we plot the mean z -position and the MSD, respectively, which both increase with increasing angular speed. In both cases we find that the numerical simulations agree well with the analytical results, cf. the third component of Eq. 15 and Eq. 12. The plots show that if the particle travels on a helix (case $\alpha = \pi/4$, cf. dashed lines in Fig. 3a,b) with the same speed as a non-rotating particle traveling in a straight fashion, if it turns sufficiently fast (i.e. if the helix is sufficiently tightly wound) it travels further from the origin on average at long time scales. Therefore a helical trajectory can be "straighter than a straight line".

The long time behavior is described by the effective diffusion constant Eq. 14, which has a complicated dependence on Ω_0 , k and h through λ . In Fig. 3c we see that at constant OU potential strength k , D increases with higher angular speed Ω_0 , as this suppresses deviations of the helical axis. This effect becomes more pronounced for higher noise amplitude h , i.e. at higher noise, the stabilizing effect of rotation is more pronounced. Increasing effective diffusion by introducing rotation or equivalently chirality is strikingly different from known examples. In 2D, chirality reduces long-time diffusion by enforcing circular turning [33, 56]. Similarly, a 3D active Brownian particle with external torque

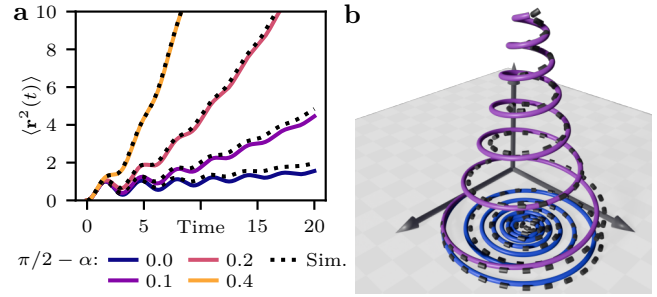


FIG. 4. **a**: Mean squared displacement for α close to $\pi/2$, such that the particles are close to describing circles, with $k = 1$, $h = 0.5$, $\Omega_0 = 2$. Black dotted lines are averages from numerical simulations. **b**: Theoretical expectation value (Eq. 15) for two values of α in color.

exhibits reduced long-time diffusion [26].

We can also study the short time behavior. Fig. 4a shows that at short times, the MSD of a helix grows slower, because it is curving back onto itself, depending on the pitch of the helix defined by the angle α . For $\alpha = \pi/2$, the MSD shows strong oscillations, as the mean position, see Fig. 4b, describes a planar inward spiral due to the influence of noise that diverts it from the circle of a noise-free particle. For smaller α , the spiral gets the 3D structure of a logarithmic spiral on a radical surface as found in Eq. 15, with both cases showing good agreement between the numerical and analytical results.

Finally, we can use our measured trajectories for malaria parasites in hydrogels to extract their MSD (Fig. 5a, averaged from 140 trajectories) and fit it with our model prediction of Eq. 12. In general, we find good

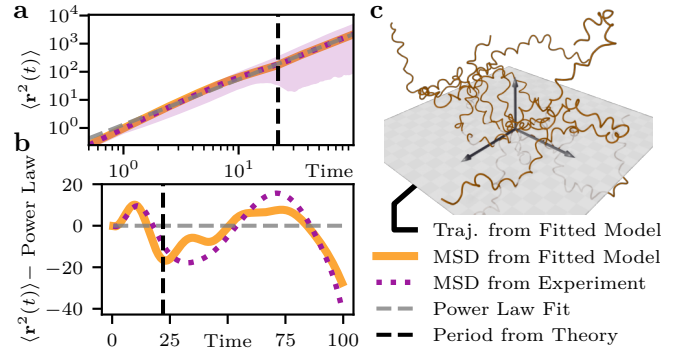


FIG. 5. **a**: Log-log plot of the mean squared displacement extracted from observed malaria parasite trajectories shown in Fig. 1 (purple, dotted), with five percent percentiles (purple, shaded) and the fitted model (orange). The gray dashed line is a fitted power law. **b**: Deviation of experiment and model from fitted power law. The vertical dashed line marks one period of rotation as extracted from the fitted model. **c**: After fitting the parameters of our model to the mean squared displacement obtained from the experiments, we can square trajectories resembling the ones extracted from experiments (cf. Fig. 1).

agreement. Our theory successfully describes the first two extrema in the deviation of the MSD from a power law (Fig. 5b), corresponding to the first turn of the helix. Our theory also predicts some effects of second and third turns visible in the MSD deviation, which are not observable in the experimental data, most likely because the biological population has a distribution of helical pitches and radii such that the later turns cannot be resolved in the average. From the fitted model parameters (Appendix E), we can derive estimates for pitch and radius of the helical trajectories as $13.2 \mu\text{m}$ and $2.8 \mu\text{m}$, respectively, well within the observed range [13]. Trajectories simulated with the fitted parameters (Fig. 5c) visually resemble the observed trajectories from Fig. 1.

In summary, our results suggest that helical trajectories provide an evolutionary advantage for swimming or gliding microorganisms with noisy force generation to effectively cover distance more quickly than when going straight. In the future, our model could guide the design of micro- and nanobots [57, 58], for example in medical applications where enhanced persistence of motion is required [59].

Acknowledgments: This work was funded by the Deutsche Forschungsgemeinschaft (DFG, German Research Foundation) through Priority Programme 2332 (Projektnummer 492010213) and Collaborative Research Center 1129 (Projektnummer 240245660).

Data availability: The code used to simulate the model, as well as python implementations of the analytical solutions for comparison are available in the following repository: GITHUB URL UPON PUBLICATION

* schwarz@thphys.uni-heidelberg.de

- [1] J. G. Mitchell and K. Kogure, Bacterial motility: links to the environment and a driving force for microbial physics, *FEMS Microbiol. Ecol.* **55**, 3 (2006).
- [2] J. M. Keestra, F. Carrara, and R. Stocker, The ecological roles of bacterial chemotaxis, *Nat. Rev. Microbiol.* **20**, 491 (2022).
- [3] K. F. Jarrell and M. J. McBride, The surprisingly diverse ways that prokaryotes move, *Nat. Rev. Microbiol.* **6**, 466 (2008).
- [4] U. S. Schwarz, Physical constraints for pathogen movement, in *Semin. Cell Dev. Biol.*, Vol. 46 (Elsevier, 2015) pp. 82–90.
- [5] D. B. Kearns, A field guide to bacterial swarming motility, *Nat. Rev. Microbiol.* **8**, 634 (2010).
- [6] L. Sibley, Intracellular parasite invasion strategies, *Science* **304**, 248 (2004).
- [7] H. S. Jennings, On the Significance of the Spiral Swimming of Organisms, *Am. Nat.* **35**, 369 (1901).
- [8] H. C. Crenshaw, A New Look at Locomotion in Microorganisms: Rotating and Translating, *Am. Zool.* **36**, 608 (1996).
- [9] H. C. Berg and L. Turner, Chemotaxis of bacteria in glass capillary arrays. *Escherichia coli*, motility, microchannel plate, and light scattering, *Biophys. J.* **58**, 919 (1990).
- [10] R. Thar and T. Fenchel, True Chemotaxis in Oxygen Gradients of the Sulfur-Oxidizing Bacterium *Thiovulum majus*, *Appl. Environ. Microbiol.* **67**, 3299 (2001).
- [11] T. Fenchel and N. Blackburn, Motile Chemosensory Behaviour of Phagotrophic Protists: Mechanisms for and Efficiency in Congregating at Food Patches, *Protist* **150**, 325 (1999).
- [12] G. Jékely, J. Colombelli, H. Hausen, K. Guy, E. Stelzer, F. Nédélec, and D. Arendt, Mechanism of phototaxis in marine zooplankton, *Nature* **456**, 395 (2008).
- [13] J. Ripp, J. Kehrer, X. Smyrnakou, N. Tisch, J. Tavares, R. Amino, C. Ruiz de Almodovar, and F. Frischknecht, Malaria parasites differentially sense environmental elasticity during transmission, *EMBO Mol. Med.* **13**, e13933 (2021).
- [14] Z. Liu, S. Li, P. Anantha, T. Thanakornsombut, L. Wu, J. Chen, R. Tsuchiya, A. K. Tripathi, Y. Chen, and I. Barman, Plasmodium sporozoite shows distinct motility patterns in responses to three-dimensional environments, *iScience* **27** (2024).
- [15] L. Lettermann, F. Ziebert, and U. S. Schwarz, A geometrical theory of gliding motility based on cell shape and surface flow, *Proc. Natl. Acad. Sci.* **121**, e2410708121 (2024).
- [16] H. C. Berg and E. M. Purcell, Physics of chemoreception, *Biophys. J.* **20**, 193 (1977).
- [17] H. C. Berg, *Random walks in biology* (Princeton University Press, 1993).
- [18] O. Pohl, M. Hintsche, Z. Alirezaeizanjani, M. Seyrich, C. Beta, and H. Stark, Inferring the chemotactic strategy of *p. putida* and *e. coli* using modified kramers-moyal coefficients, *PLoS Comput. Biol.* **13**, e1005329 (2017).
- [19] P. Romanczuk, M. Bär, W. Ebeling, B. Lindner, and L. Schimansky-Geier, Active Brownian particles, *Eur. Phys. J. Spec. Top.* **202**, 1 (2012).
- [20] C. Bechinger, R. Di Leonardo, H. Löwen, C. Reichhardt, G. Volpe, and G. Volpe, Active Particles in Complex and Crowded Environments, *Rev. Mod. Phys.* **88**, 045006 (2016).
- [21] A. Zöttl and H. Stark, Emergent behavior in active colloids, *J. Phys. Condens. Matter.* **28**, 253001 (2016).
- [22] B. Liebchen and D. Levis, Chiral active matter, *Europhys. Lett.* **139**, 67001 (2022).
- [23] J. R. Howse, R. A. L. Jones, A. J. Ryan, T. Gough, R. Vafabakhsh, and R. Golestanian, Self-Motile Colloidal Particles: From Directed Propulsion to Random Walk, *Phys. Rev. Lett.* **99**, 048102 (2007).
- [24] D. Debnath, P. K. Ghosh, Y. Li, F. Marchesoni, and B. Li, Diffusion of eccentric microswimmers, *Soft Matter* **12**, 2017 (2016).
- [25] J. R. Gomez-Solano, A. Blokhuis, and C. Bechinger, Dynamics of Self-Propelled Janus Particles in Viscoelastic Fluids, *Phys. Rev. Lett.* **116**, 138301 (2016).
- [26] F. J. Sevilla, Diffusion of active chiral particles, *Phys. Rev. E* **94**, 062120 (2016).
- [27] J. R. Gomez-Solano and F. J. Sevilla, Active particles with fractional rotational Brownian motion, *J. Stat. Mech. Theor. Exp.* **2020**, 063213 (2020).
- [28] A. R. Sprenger, L. Caprini, H. Löwen, and R. Wittmann, Dynamics of active particles with translational and rotational inertia, *J. Phys. Condens. Matter.* **35**, 305101 (2023).

- [29] S. van Teeffelen and H. Löwen, Dynamics of a Brownian circle swimmer, *Phys. Rev. E* **78**, 020101 (2008).
- [30] R. Ledesma-Aguilar, H. Löwen, and J. M. Yeomans, A circle swimmer at low Reynolds number, *The European Physical Journal E* **35**, 70 (2012).
- [31] F. Kümmel, B. ten Hagen, R. Wittkowski, I. Buttinoni, R. Eichhorn, G. Volpe, H. Löwen, and C. Bechinger, Circular Motion of Asymmetric Self-Propelling Particles, *Phys. Rev. Lett.* **110**, 198302 (2013).
- [32] N. A. Marine, P. M. Wheat, J. Ault, and J. D. Posner, Diffusive behaviors of circle-swimming motors, *Phys. Rev. E* **87**, 052305 (2013).
- [33] H. Löwen, Chirality in microswimmer motion: From circle swimmers to active turbulence, *Eur. Phys. J. Spec. Top.* **225**, 2319 (2016).
- [34] A. Nourhani, S. J. Ebbens, J. G. Gibbs, and P. E. Lammert, Spiral diffusion of rotating self-propellers with stochastic perturbation, *Phys. Rev. E* **94**, 030601 (2016).
- [35] L. Caprini, H. Löwen, and U. M. B. Marconi, Chiral active matter in external potentials, *Soft Matter* **19**, 6234 (2023).
- [36] B. Lindner, Diffusion of particles subject to nonlinear friction and a colored noise, *New J. Phys.* **12**, 063026 (2010).
- [37] P. K. Ghosh, Y. Li, G. Marchegiani, and F. Marchesoni, Communication: Memory effects and active Brownian diffusion, *J. Chem. Phys.* **143**, 211101 (2015).
- [38] N. Narinder, C. Bechinger, and J. R. Gomez-Solano, Memory-Induced Transition from a Persistent Random Walk to Circular Motion for Achiral Microswimmers, *Phys. Rev. Lett.* **121**, 078003 (2018).
- [39] P. Bayati and A. Nourhani, Memory effects in spiral diffusion of rotary self-propellers, *Phys. Rev. E* **105**, 024606 (2022).
- [40] A. R. Sprenger, S. Jahanshahi, A. V. Ivlev, and H. Löwen, Time-dependent inertia of self-propelled particles: The Langevin rocket, *Phys. Rev. E* **103**, 042601 (2021).
- [41] R. Wittkowski and H. Löwen, Self-propelled Brownian spinning top: Dynamics of a biaxial swimmer at low Reynolds numbers, *Phys. Rev. E* **85**, 021406 (2012).
- [42] B. M. Friedrich and F. Jülicher, The stochastic dance of circling sperm cells: sperm chemotaxis in the plane, *New J. Phys.* **10**, 123025 (2008).
- [43] B. M. Friedrich and F. Jülicher, Steering Chiral Swimmers along Noisy Helical Paths, *Phys. Rev. Lett.* **103**, 068102 (2009).
- [44] G. Szamel, Self-propelled particle in an external potential: Existence of an effective temperature, *Phys. Rev. E* **90**, 012111 (2014).
- [45] F. J. Sevilla, R. F. Rodríguez, and J. R. Gomez-Solano, Generalized Ornstein-Uhlenbeck model for active motion, *Phys. Rev. E* **100**, 032123 (2019).
- [46] E. Woillez, Y. Kafri, and V. Lecomte, Nonlocal stationary probability distributions and escape rates for an active Ornstein-Uhlenbeck particle, *J. Stat. Mech. Theor. Exp.* **2020**, 063204 (2020).
- [47] D. Martin, J. O’Byrne, M. E. Cates, E. Fodor, C. Nardini, J. Tailleur, and F. van Wijland, Statistical mechanics of active Ornstein-Uhlenbeck particles, *Phys. Rev. E* **103**, 032607 (2021).
- [48] D. Martin and T. A. d. Pirey, AOUP in the presence of Brownian noise: a perturbative approach, *J. Stat. Mech. Theor. Exp.* **2021**, 043205 (2021).
- [49] G. H. P. Nguyen, R. Wittmann, and H. Löwen, Active Ornstein-Uhlenbeck model for self-propelled particles with inertia, *J. Phys. Condens. Matter.* **34**, 035101 (2021).
- [50] A. Crisanti and M. Paoluzzi, Most probable path of active Ornstein-Uhlenbeck particles, *Phys. Rev. E* **107**, 034110 (2023).
- [51] S. Dutta, Most probable paths for active Ornstein-Uhlenbeck particles, *Phys. Rev. E* **107**, 054130 (2023).
- [52] J. H. Fritz and U. Seifert, Thermodynamically consistent model of an active Ornstein-Uhlenbeck particle, *J. Stat. Mech. Theor. Exp.* **2023**, 093204 (2023).
- [53] C. Weber, P. K. Radtke, L. Schimansky-Geier, and P. Hänggi, Active motion assisted by correlated stochastic torques, *Phys. Rev. E* **84**, 011132 (2011).
- [54] J. Bradbury, R. Frostig, P. Hawkins, M. J. Johnson, C. Leary, D. Maclaurin, G. Necula, A. Paszke, J. VanderPlas, S. Wanderman-Milne, and Q. Zhang, JAX: composable transformations of Python+NumPy programs (2018).
- [55] P. Kidger, *On Neural Differential Equations*, PhD Thesis, University of Oxford (2021).
- [56] K. S. Olsen and H. Löwen, Optimal diffusion of chiral active particles with strategic reorientations, *Phys. Rev. E* **110**, 064606 (2024).
- [57] A. Ghosh and P. Fischer, Controlled Propulsion of Artificial Magnetic Nanostructured Propellers, *Nano Lett.* **9**, 2243 (2009).
- [58] T. Yamamoto and M. Sano, Chirality-induced helical self-propulsion of cholesteric liquid crystal droplets, *Soft Matter* **13**, 3328 (2017).
- [59] J. Llacer-Wintle, A. Rivas-Dapena, X.-Z. Chen, E. Pellicer, B. J. Nelson, J. Puigmartí-Luis, and S. Pané, Biodegradable small-scale swimmers for biomedical applications, *Adv. Mater.* **33**, 2102049 (2021).

END MATTER

Appendix A - Experimental protocol: Malaria is caused by unicellular parasites of the genus *Plasmodium*. During its complex life cycle, the sporozoite, a 10 μm long, crescent shaped motile stage of the parasite, is transmitted from a mosquito during its blood meal and utilizes rapid gliding motility to migrate into blood vessels. The experimental setup [13] consists of a soft and porous polyacrylamide hydrogel serving as 3D

substrate mimicking the host skin. A mosquito salivary gland infected by *P. berghei* sporozoites that express a fluorescent protein in their cytoplasm was placed on top of the gel, such that sporozoites could invade into the gel at high numbers. 3D sporozoite migration was observed using spinning disc confocal microscopy, which allowed us to follow the rapid migration of hundreds of parasites.

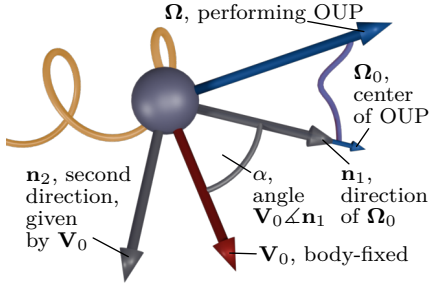


FIG. A1. Model schematics. The translational velocity \mathbf{V}_0 is fixed in the body frame, but the angular velocity $\boldsymbol{\Omega}$ performs an Ornstein-Uhlenbeck process (OUP) centered around the body fixed $\boldsymbol{\Omega}_0$. The body coordinates are given by the vectors \mathbf{n}_1 , the direction of the average angular velocity $\boldsymbol{\Omega}_0$, and \mathbf{n}_2 , chosen such that \mathbf{V}_0 is in the plane spanned by $\mathbf{n}_1, \mathbf{n}_2$, with an angle of α between \mathbf{V}_0 and \mathbf{n}_1 ,

The microscopy results were processed by an automated image analysis pipeline. Standard filtering and registration approaches were combined with a custom build deconvolution and tracking pipeline to obtain 3D trajectories of individual sporozoites.

Appendix B - Truncation for $\Omega_0 = 0$: The truncation presented above breaks down for $\Omega_0 = 0$, because the equation for $\boldsymbol{\Omega}$ decouples from the rest, and $\langle \boldsymbol{\Omega} \rangle$ is dominated by the mean squared displacement (MSD) of the OUP instead of Ω_0 . However, in the limit of small noise ($h^2 \ll k^3$), the previously derived eigenvalue (Eq. 10) has a well-defined limit

$$\lambda \Big|_{\Omega_0=0} \approx -\frac{h^2}{k^2}. \quad (16)$$

Following through the previous derivation of Eq. 9 for the case of $\Omega_0 = 0$, and truncating $\langle \boldsymbol{\Omega} \times (\boldsymbol{\Omega} \times (\boldsymbol{\Omega} \times \mathbf{n}_1)) \rangle \approx -h^2/(2k) \langle \boldsymbol{\Omega} \times \mathbf{n}_1 \rangle$, using the MSD of the OUP instead of Ω_0^2 , we find the same result. Therefore, even if the original derivation is not valid, the eigenvalue as written correctly includes the $\Omega_0 \rightarrow 0$ limiting case. This is also confirmed by the numerical simulations for the $\Omega_0 = 0$ case in Fig. 3.

Appendix C - Decorrelation of body-frame: We want to find the decorrelation of $\langle \mathbf{n}_2 \rangle$ in the regime where $\boldsymbol{\Omega}_0$ dominates the noise of the OUP. From the previous solution, Eq. 7, we obtain

$$d \langle \mathbf{n}_1 \rangle = \langle \boldsymbol{\Omega} \times \mathbf{n}_1 \rangle dt = -\lambda \langle \mathbf{n}_1 \rangle dt. \quad (17)$$

The analogous equation for \mathbf{n}_2 can be expanded by introducing the vector \mathbf{n}_3 , which expands \mathbf{n}_1 and \mathbf{n}_2 to an orthonormal basis, and using the Jacobi identity,

$$\begin{aligned} d \langle \mathbf{n}_2 \rangle / dt &= \langle \boldsymbol{\Omega} \times \mathbf{n}_2 \rangle = \langle \boldsymbol{\Omega} \times (\mathbf{n}_3 \times \mathbf{n}_1) \rangle \\ &= -\langle \mathbf{n}_3 \times (\mathbf{n}_1 \times \boldsymbol{\Omega}) \rangle - \langle \mathbf{n}_1 \times (\boldsymbol{\Omega} \times \mathbf{n}_3) \rangle \end{aligned} \quad (18)$$

In the first term, we can write $\mathbf{n}_1 \times \boldsymbol{\Omega} = \langle \mathbf{n}_1 \times \boldsymbol{\Omega} \rangle + \boldsymbol{\Delta}$, where by rotational symmetry $\boldsymbol{\Delta}$ is isotropic in the x, y -plane, and hence $\langle \mathbf{n}_3 \times \boldsymbol{\Delta} \rangle = 0$, such that with the previous result

$$-\langle \mathbf{n}_3 \times (\mathbf{n}_1 \times \boldsymbol{\Omega}) \rangle = -\langle \mathbf{n}_3 \times (\lambda \langle \mathbf{n}_1 \rangle) \rangle = -\lambda \langle \mathbf{n}_2 \rangle, \quad (19)$$

where the last steps follows a similar argument (introducing a isotropic $\boldsymbol{\Delta}$ computing the cross product $\mathbf{n}_3 \times \mathbf{n}_1 = \mathbf{n}_2$ through the averages. For the second term, similar logic can be applied, yielding

$$\begin{aligned} -\langle \mathbf{n}_1 \times (\boldsymbol{\Omega} \times \mathbf{n}_3) \rangle &= -\langle \mathbf{n}_1 \times (\boldsymbol{\Omega} \times (-\mathbf{n}_2 \times \mathbf{n}_1)) \rangle \\ &= -\langle \mathbf{n}_1 \times (\mathbf{n}_2 \times (\mathbf{n}_1 \times \boldsymbol{\Omega})) \rangle - \langle \mathbf{n}_1 \times (\mathbf{n}_1 \times (\boldsymbol{\Omega} \times \mathbf{n}_2)) \rangle \\ &= -\lambda \langle \mathbf{n}_2 \rangle - \langle \mathbf{n}_1 \times (\mathbf{n}_1 \times (\boldsymbol{\Omega} \times \mathbf{n}_2)) \rangle. \end{aligned} \quad (21)$$

Now, with an analogous argument as used in the truncation in deriving Eq. 9, for the last term in Eq. 21 only the \mathbf{n}_1 orthogonal part of $\boldsymbol{\Omega} \times \mathbf{n}_2$ is relevant, which is generated by the \mathbf{n}_1 parallel component of $\boldsymbol{\Omega}$. We approximate this as $\boldsymbol{\Omega}^{\parallel} \approx \Omega_0 \mathbf{n}_1$ to obtain

$$-\langle \mathbf{n}_1 \times (\mathbf{n}_1 \times (\boldsymbol{\Omega} \times \mathbf{n}_2)) \rangle = \Omega_0 \langle \mathbf{n}_3 \rangle, \quad (22)$$

which ultimately combines to

$$d \langle \mathbf{n}_2 \rangle / dt = -2\lambda \langle \mathbf{n}_2 \rangle + \Omega_0 \langle \mathbf{n}_3 \rangle. \quad (23)$$

An analogous equation can be derived for $\langle \mathbf{n}_3 \rangle$, giving precisely decay with two times the original eigenvalue λ while rotating with angular speed Ω_0 . The two terms in the expansion of Eq. 20 can be interpreted as the aforementioned decorrelation of the plane on the one hand, and rotation and decorrelating within the plane on the other hand.

Appendix D - Derivation of MSD: The MSD can now be obtained by first computing it from the formal solution

$$\mathbf{r}(t) = \int_0^t dt (\cos(\alpha) \mathbf{n}_1 + \sin(\alpha) \mathbf{n}_2), \quad (24)$$

which yields

$$\begin{aligned} \langle \mathbf{r}(t)^2 \rangle &= \int_0^t ds_1 \int_0^t ds_2 \left(\cos^2(\alpha) \langle \mathbf{n}_1(s_1) \cdot \mathbf{n}_1(s_2) \rangle \right. \\ &\quad \left. + \sin^2(\alpha) \langle \mathbf{n}_2(s_1) \cdot \mathbf{n}_2(s_2) \rangle \right), \end{aligned} \quad (25)$$

where the mixed terms vanish, as due to their perpendicularity and the rotational symmetry the expectation value of their scalar products has to be zero even if evaluated at different times. The remaining correlation functions can be directly obtained from the solutions obtained for $\langle \mathbf{n}_1 \rangle$ and $\langle \mathbf{n}_2 \rangle$ as

$$\langle \mathbf{n}_1(s_1) \cdot \mathbf{n}_1(s_2) \rangle = e^{\lambda|s_1-s_2|}, \quad (26)$$

$$\langle \mathbf{n}_2(s_1) \cdot \mathbf{n}_2(s_2) \rangle = \cos(\Omega_0|s_1-s_2|) e^{2\lambda|s_1-s_2|}, \quad (27)$$

such that we finally compute the MSD by simple integration.

Appendix E - Fitted Parameters: The sporozoites observed don't move at a constant speed, and even their average speed can vary between different parasites by a factor of 3. For this analysis, we resampled the trajectories assuming a constant speed of $1 \mu\text{m/s}$. The fit of the

MSD in Fig. 5 results in the following parameters:

TABLE I. Results for fitting the model to the MSD computed from observed and resampled trajectories of malaria parasites.

Parameter	Ω_0	α	θ	h
Fit Result	0.285 1/s	0.926	1.078 1/s	0.154 1/s ^{3/2}